Suitably impressive thesis title

Donovan Webb

St Peter's College

University of Oxford

A thesis submitted for the degree of

Doctor of Philosophy

Trinity 2025

Contents

Appendices

1
Motivation

2

Ion Trap Apparatus

Contents

A vast effort is spent on the initial build-up of the an ion trap system, but throughout the life of the experiment, a greater effort is spent on its daily maintenance. I hope that this chapter will serve as a useful debugging-resource for future members of the FastGates team, and as a detailed recipe for anyone building a similar system.

Due to the size and complexity of the system, we introduce an inital overview of the design, motivated by the desired functions. Many such ion trap experiment overviews exist in the theses of previous PhD generations, and so we will attempt to limit the discussion here to the unique features and capabilities of our system.
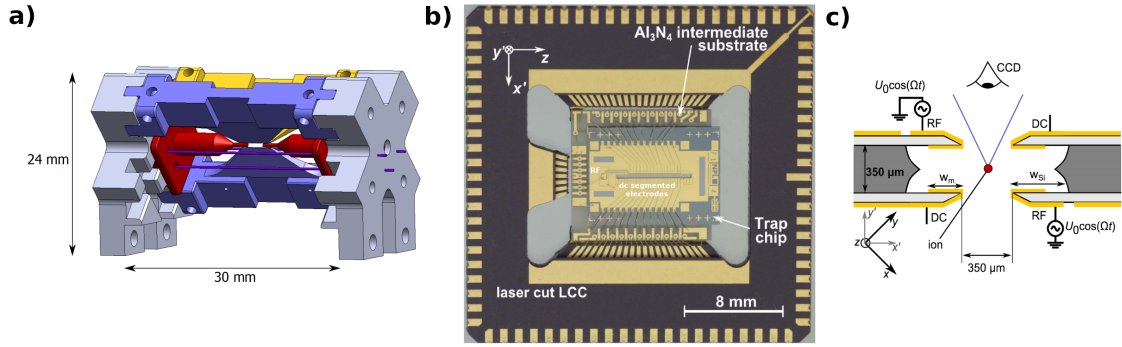
Figure 2.1: a) XX Place holder figure. **b)** The NPL trap in use in this thesis. This is a microfabricated, segmented, multilayer trap. **c)** A cross sectional view of the NPL trap showing the RF and DC electrode positions. Figures from [1].

However, as a short introduction we state the aim of an ion trap is of course to trap ions! This is achieved by static and dynamic electric fields which, due to the ions possesing non-zero electric charge, can provide trapping potentials, section 2.1. Due to the fragility of the internal states of the ion (these are state of the art sensors after all), we must take great care in isolating the ion from any noisy environment. This neccesitates the use of ultra-high vacuum (UHV) systems, section 2.3, vibration isolation, and magnetic shielding, section 2.2. To manipulate the internal electronic states of the ion, we create local electric and magnetic fields using RF antennae and, in this work, lasers, sections 2.4 and 2.4.1. Finally, to interface with the apparatus we have built, at the time scales set by our interaction strengths, we require a sophisticated and custom control system which is discussed in section **??**.

2.1 The Ion Trap

To create trapping potentials we use linear Paul traps, a schematic of such is shown in Figure 2.1 (a). As explained by Earnshaw's theorem, ($\nabla^2 V = 0$), a stable stationary point in 3D can not be realized using only static electric potentials, V, as if the potential is confining in two dimensions, it will be anticonfining in the third. Therefore, to achieve stable trapping either an oscillating electric field (Paul trap [**XXX**]), or a static magnetic field (Penning traps [**XXX**]) must be utilized to create a confining pseudopotential.

Recently, the microfabricated surface style linear Paul trap has gained popularity due to the maturity of chip fabrication technologies [2] and the potential route to scalability this offers. In the surface trap, the 3D radial and axial electrodes of a "macro" trap are effectively projected onto a 2D surface. The stable point of such a trap is typically on the order of 50 μm from the chip surface. The ease of fabrication of surface traps has allowed the creation of complex multizone devices with many DC electrodes. These multizone traps enable the shuttling of ions, a requirement for Quantum CCD type architectures [3]. However, this surface style geometry typically come with two costs: the depth of the trapping potential is often greatly reduced, and the close proximity of the surface to the ion can be a large contributor to motional heating rates [4].

The *NPL* microfabricated 3D trap [5, 6], as is used in our experiment, brings together the advantages of chip fabrication as well as the low heating rates and high trapping depths of a 3D style trap with greater ion-surface distances. This is achieved by a multilayer chip as shown in Figure 2.1 (b, c). The radial trapping is provided by RF rails on opposite diagonals of the slit whilst axial trapping may be realized by the numerous DC electrodes. The ion-surface distance is now of the order 250 μm and we have demonstrated heating rates of 33(3) q/s on a 4 MHz radial mode (see section 3.3.2).

We aim for an axial ion separation of around 5 μm which, for ^{40}Ca$^+$ ions means a trapping potential of $\omega_z \approx 2\pi \cdot 1.6$ MHz. This ion separation was chosen to reduce the cross talk between ions when singly addressed (see section 2.4.2).

We are targeting approximately 5 MHz for our radial frequencies, as we shall use radial addressing for two-qubit entangling gates. The choice of this higher frequency is motivated by several factors. The Doppler cooling limit ($\overline{n} = \Gamma/\omega$, where Γ is the transition linewidth and ω is the frequency of the cooled mode) inversely scales with the mode frequency. Consequently, higher mode frequencies result in lower temperatures following initial cooling. Additionally, a higher center-of-mass radial mode enables greater frequency separation of radial modes in a multi-ion crystal, which allow for greater selectivity of participating modes.

Using the pseudopotential approximation [7] for the confining field, we can find a trapping frequency in one radial direction ω_p

$$\omega_p = \frac{e\alpha V_{RF}}{\sqrt{2}\Omega_{RF}M\rho^2},$$ (2.1)

where α is a factor of order unity given by the geometry of the trap, V_{RF} and Ω_{RF} are the voltage and frequency provided to the RF-electrode, M is the mass of the ion, and ρ is the ion-RF electrode separation. Applying some DC voltage on the axial electrodes leads to axial confinement with frequency ω_{ax}, but must defocus the radial confinements as the total curvature of the pseudopotential must remain constant,

$$\omega_{rad} = \sqrt{\omega_p^2 - \omega_{ax}^2/2}.$$ (2.2)

Due to the geometry of the DC electrodes with respect to the ion chain, the *NPL* trap focuses one of the radial modes and defocuses the other when the DC electrodes are increased,

$$\omega_{rad\pm} = \sqrt{\omega_p^2 - (1 \mp \beta)\omega_{ax}^2/2},$$ (2.3)

where β is some factor due to the geometry of this geometry. From simulation $\beta > 1$ for $\Omega_{RF} = 2\pi \cdot 23$ MHz and $V_{RF} = 200$ V and so one radial mode increases with DC voltage applied and one decreases.

	V_{RF}/V	V_{DC}/V	$\Omega_{RF}/(2\pi\cdot\text{MHz})$	$\omega/(2\pi\cdot\text{MHz})$		q
				ω_{ax}	ω_{rad}	
Experiment	200	-7	23	1.6	4.9	0.61
Loading	100	-2	23	0.8	2.0	0.25

Table 2.1: Simulated trapping parameters for both "Experiment" and "Loading" settings $^{40}\text{Ca}^+$ with the NPL trap. The "Experiment" setting is optimized for high axial mode frequencies whilst the "Loading" setting maintains a lower q factor for practical loading.

A possible set of parameters to achieve $\omega_{ax} = 2\pi \cdot 1.6$ MHz and $\omega_{rad+} = 2\pi \cdot 4.9$ MHz can be seen in the "Experiment" trapping in Table 2.1.

From the Mathieu equations, the areas of stability depend upon a factor q [8], where $q = 2\sqrt{(}2)\omega/\Omega_{RF}$. Generally, we require q to be as low ($q < 0.3$) for convenient

trapping. To satisfy this requirement a "Loading" setting (with parameters in table 2.1) may be used with $q = 0.25$ and then the V_{RF} ramped to the "Experiment" trapping for high radial mode frequencies.

2.1.1 Trap RF Chain

To utilise radial motional modes for low error quantum gates, we require the radio frequency (RF) field that produces the desired trapping pseudopotential to be both frequency and amplitude stable. Our *NPL* trap is rated for a max peak-to-peak voltage of 400 Vpp on the RF electrodes. Here we describe the elements of the "RF chain" that supplies this voltage, as shown in figure **??**.

Our frequency source is a DDS-based synthesiser, named *Urukul*, part of the *Artiq Sinara* [**XXX**] hardware ecosystem. We operate the *Urukul* at max output power, +10 dBm and with a frequency around 27.8 MHz. This signal is then fed to an "ultra-low noise limiting amplifier" named *Squareatron* [**XXX**]. The purpose of *Squareatron* is to greatly reduce the amplitude noise of the RF signal, V_{RF}, which is key to low radial mode frequency drifts as can be seen by the linear relationship between trapping frequency and V_{RF} in equation 2.1. The *Squareatron* outputs +17.4 dBm, which we subsequently attenuate by 19.5 dB. We then amplify the signal by a further 33.7 dB using a *Mini-Circuits ZHL-1-2W-S+*, high power amplifier. We now have +32 dBm RF power to drive the trap electrodes, however we need to match the current 50 Ω impedance to the small capacitance of the trap electrodes. To do this, we use an LC impedance matching circuit with tuned resonant frequency of 27.84 MHz, and a measured Q factor of 43.8 (found by fitting S11 impedance measurements). This resonant circuit has three main effects: it ensures good power transfer between RF input and trap electrodes via impedance matching, it steps up the voltage to the required 400 Vpp, and it filters out unwated harmonics due to the bandpass nature of the LC circuit.

If components are chosen correctly, and adequately protected from environmental noise, this chain can produce the desired frequency and amplitude stable RF we require. Characterisations of the motional mode stability are discussed in section **??**.

We are still yet to fully quantify and debug the motional stability against thermal and mechanical noise, however it should be noted that other groups do opt for active stabilisation of RF amplitude through closed feedback loops [**XXX**].

2.2   Magnetic Field

Stable Zeeman shifts of the ion energy levels are required for long spin coherence times (see section 3.2.2), and for low error single and two qubit gates. We use a permanent magnet array of Samarium Cobalt, Sm_2Co_17, in a Helmholtz configuration to create a stable magnetic field of 5.4 G. Samarium Cobalt was chosen for its low temperature coefficient of remenance, -0.03%/K.

The ion is shielded from unwanted external magnetic fields by two layers of 3 mm thick MuMetal shielding from *MagneticShields*. The factory quoted shielding factor is 546 for DC fields. Spin coherence time comparisons for the ion with and without magnetic shielding are shown in section 3.2.2.

2.3   Vacuum System and Beam Geometry

Ultra High Vacuum (UHV) is required to extend the ion storage lifetime. However, UHV equipment is often bulky, and puts constraints on the access and visibility of the ion chain. Here we describe the designed vacuum system, and beam access. The vacuum system and beam geometries were designed by Sebastian Saner and Mariella Minder, and constructed by Sebastian Saner, Fabian Pokorny, and myself.

We aim for a residual pressure of $< 10^{-11}$ mbar. For this strict requirement, we must take care in selecting in-vacuum materials, and follow thorough cleaning and baking procedures. A summary of tactics that were useful in the construction of the vacuum system can be found in [9, 10].

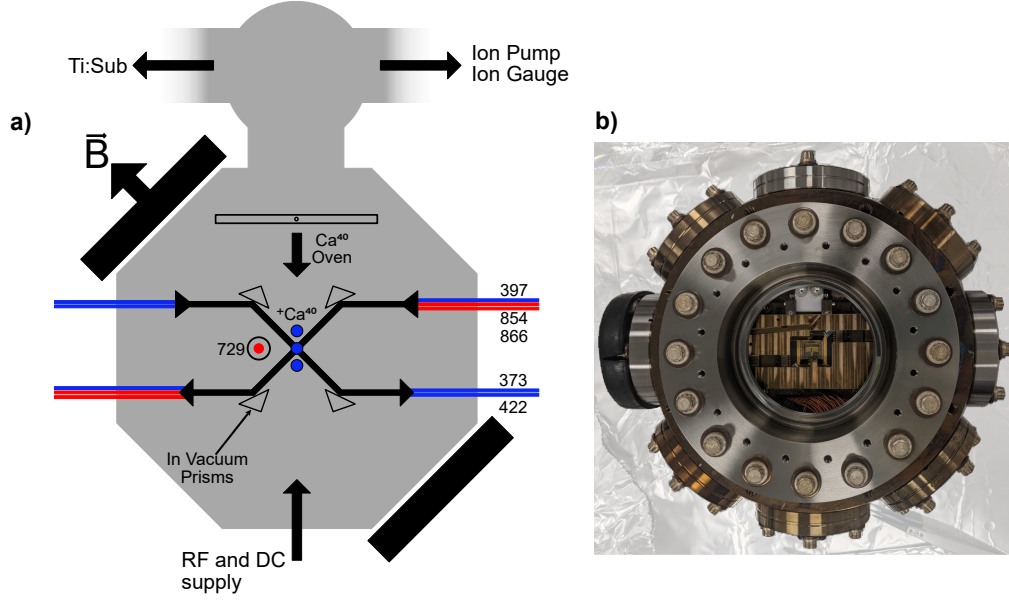A schematic and photograph of the vacuum system can be seen in Figure 2.2.

Figure 2.2: a) XXX Place holder figure. A schematic of the vacuum chamber. Wavelengths apart from 729-nm enter through the side CF40 viewports and are directed onto the ions by in vacuum prisms. The 729-nm light enters through the larger CF100 viewports. **b)** A photograph of the assembled system prior to baking.
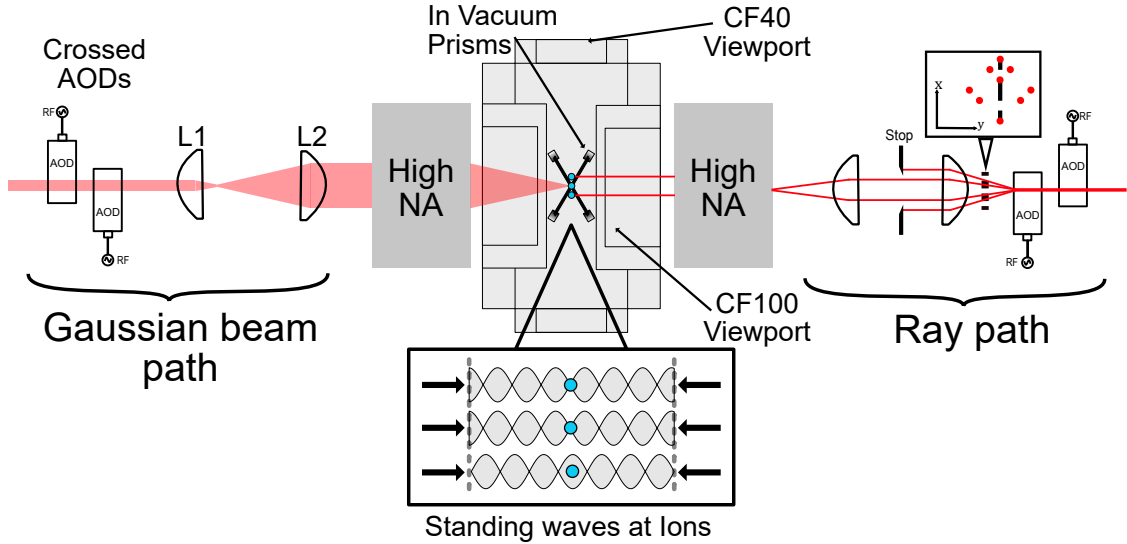
Figure 2.3: XXX Place holder figure. The standing wave single addressing system. Dual high NA objectives focus the light to a tight waist at the ions location. AODs are used to steer the light to only selected ions. The left hand side of the figure shows the Gaussian profile of the light, whilst the right hand side shows a ray representation of how two singly addressing spots are formed at the ions. L1 is a telecentric scanning lens and in combination with L2 form a beam expander.

The system consists of a 6" spherical-octagonal experimental chamber[1] connected to a spherical chamber with ion pump[2], ion gauge[3] and Titanium sublimator pump (TSP)[4] attached. The ion pump and TSP maintain the UHV to the desired $< 10^{-11}$ mbar. We find that on the ion pump alone we cannot maintain UHV indefinitely, however, firing the TSP every 4 weeks with 41 A for 60 seconds provides a sufficient pumping rate. At the time of system baking, we performed a He leak test, but did not find any external leaks. We suspect the gradual pressure increase is either due to our use of in-vacuum optics, optics epoxy adhesive[5], or our use of soldered PCB components.

For optical access we have two recessed CF100 viewports[6] on the two large faces of the experiment can. We require recessed viewports due to our chosen main objectives[7]. These custom objectives have an effective focal length of 33 mm, a working distance of 24.4 mm, and a numerical aperture of 0.6. They are coated for 397-nm and 729-nm. The consideration for dual high NA objectives is relatively unique in ion trap experiments, and was mainly motivated by previous work on fast entangling gates via standing waves [11].

There is further optical access via two CF40 side viewports[8] coated for 397-nm, 422-nm, 729-nm, 854-nm and 866-nm. Due to the spatial constraints from the trap assembly and high NA objectives, we require multiple of our beam to enter the vacuum can through these side ports. For the ion chain to be visible from these side ports we use in vacuum dielectric mirrors. These fuse-silica mirrors are UHV rated and coated for 372-nm, 397-nm, 422-nm, 729-nm, 854-nm and 866-nm, with reflectivities of >99% for both s- and p-polarised light. Figure 2.2 shows a schematic of the beam geometries via the side ports. A limitation of this beam geometry is that due to the permanent B-field direction, we are unable to apply pure π or $\sigma_{\pm}$

---

[1]Kimball MCF600-SphOct-F2C8
[2]Agilent VacIon Plus 20 Pump
[3]Agilent UHV-24P Ion gauge
[4]Scanwel custom housing
[5]EPO-TEK 353ND
[6]UK Atomic Energy Authority P/N VPR100015
[7]Photon Gear custom Atom Imager
[8]LewVac ZFSVP-DUV-40CF-OUM

light to the ion. However for applications where strict polarisation control is needed, the beams can be incident through the CF100 viewport.

We use an electrical feedthrough on a CF40 flange[9] to supply our trap chip and atomic source oven with DC and RF voltages. As the DC cables run within close proximity to the RF supply, electrical pick up is a potential issue for our DC lines. RF leaked onto our DC electrodes will create unwanted pseudopotential which can lead to unexpected mode geometries, or required compensation field. We mitigate this leakage through an in-vacuum RC low pass filter board within close proximity of the trap chip with a cutoff frequency of 17 kHz. The trap chip is mounted onto this filter board via a custom Polyether ether ketone (PEEK) interposer with electric feedthroughs via embedded *Fuzz buttons*[10].
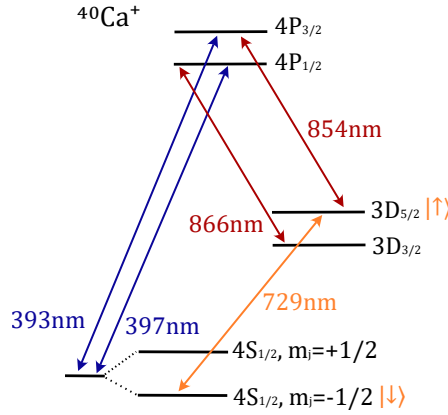
2.4   Ca$^+$ Laser Systems

Figure 2.4: Electronic energy levels of ^{40}Ca$^+$, which will be used in this thesis. The levels are split by the Zeeman effect due to a 5.4 G external magnetic field (they are shown explicitely only for the ground state). The transitions marked are required for cooling and control over the ion. We shall use the optical-qubit with a quadrupole transition at 729-nm. XXX TODO: Add zeeman levels for D5/2.

Singly-charged group 2 elements are popular in ion trap experiments due to their single outer electron resulting in Hydrogen-like energy levels. In this thesis we

---

[9]Allectra custom
[10]Custom Interconnects

use ^{40}Ca$^+$.

^{40}Ca$^+$has no nuclear spin giving the (relatively) simple level structure shown in figure 2.4. The external magnetic field of 5.4 G is applied to split the levels via the Zeeman effect. The relevant laser transitions for our planned ion trap experiment are indicated.

A zero nuclear spin isotope of calcium was chosen due to this simple level structure without hyperfine splitting. The greater number of levels due to hyperfine splitting lead to more decay paths and therefore greater complications in both cooling and gate schemes. However, this does come at the cost of no available magnetic field insensitive transitions, which are often used in ion trap experiments to further decouple the ion from a noisy environment [**<empty citation>**].

We define our qubit by the quadrupole transition at 729-nm, which we describe in the following section.

Access to other excited levels, outside of our defined two level system, are crucial for ion trap quantum logic so that we can readout the qubit with state selective fluorescence (397-nm, and 866-nm transitions) and optically pump for state preparation (397-nm, 866-nm, and 854-nm transitions). Details on these schemes are given in chapter **??**. We also require access to two additional transitions in neutral calcium for isotope selective ionisation, 422-nm and 372-nm.

These transitions (apart from the 729-nm) are all driven by diode lasers[11], which are frequency stabilised to a reference cavity[12] via Pound-Drever-Hall (PDH) locking. We require PDH locking to ensure that laser frequencies are stable to <1 MHz level, well below the natural line widths of all the dipole transitions listed above. We continuosly monitor the laser frequencies with a wavemeter[13].

Frequency and amplitude control for all lasers is achieved via acousto-optic modulators (AOMs) which are driven by Artiq integrated DDS chips, *Urukuls*. We use

---

[11]All Toptica diodes. Red lasers: MDL DL pro; Blue lasers: MDL DL pro HP; 372-nm: iBEAM-SMART-375-S

[12]Stable Laser Systems SLS-6010 4-Bore Cylindrical Cavity

[13]HighFinesse WS7

AOMs in a double pass configuration to allow shifts of the laser frequency by +/- 100 MHz, with no signicant angular shifts or loss of fibre coupling.

2.4.1   Narrow Line Width 729 Laser

Lasers are a key tool for creating the highly localised, strong electric field amplitudes and gradients needed to drive both carrier and sideband transitions of the trapped ion.

As shown in Figure 2.4, we will use two levels within the $4S_{1/2}$ to $3D_{5/2}$ manifolds to define our qubit. This is an electric quadrupole transition as $\Delta l = 2$. For the Calcium ion this transition is at 729-nm, and so we use a near resonance 729-nm laser to implement single- and multi-qubit gates (sections 3.2.4 and 3.5). We also use this transition, after Doppler cooling, for resolved sideband cooling to bring the motional mode close to its ground state (as discussed in section 3.3.1).

This transition is narrrow line width due the the long lived $3D_{5/2}$ state, and so, for power efficiency, we must use a narrow linewidth laser. For our "fast entangling gates" use case we require large electric-field intensities at the ion to drive sideband transitions, this will be discussed further in the single-addressing and two-qubit gate sections, but here it is sufficient to say we require >100 mW of light at the ion plane. Here we describe the built system consisting of a Ti:Saph laser system pumped with by an Nd:YAG 532-nm laser.

We pump an *M2 Solstis* Ti:Saph [**XXX**] with 18 W of 532-nm light from a *Coherent Verdi-V* system [**XXX**] to produce around 5W of 729-nm light. The Ti:Saph is engineered to operate with a stable < 50 kHz linewidth. Ti:Saph crystals have broadband gain profiles [**XXX**], which is often exploited in research environments to create frequency tunable laser systems. We however want a narrow linewidth, single frequency laser, and so the *Solstis* has multiple intracavity frequency selective elements. These consist of (in order of coarse frequency selectivity), a birefringent filter, a tunable Fabry-Pérot etalon, and the surrounding bow-tie cavity. For stable single mode operation, the *Solstis* employs an active "dither" servo to
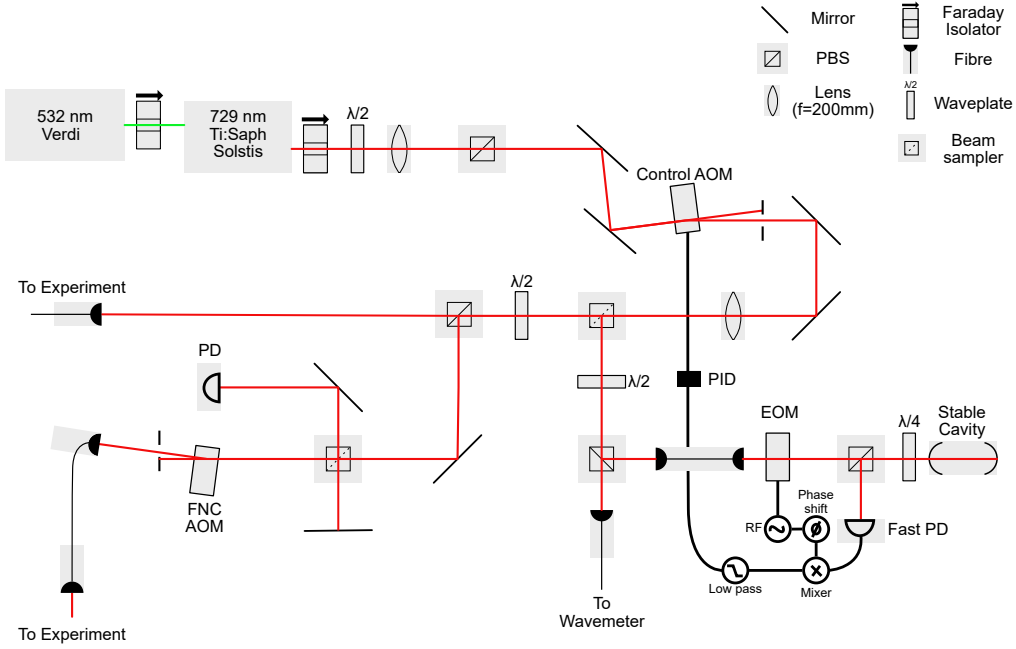
Figure 2.5: The 729-nm system. A Ti:Saph laser tuned to 729-nm is pumped by a 532-nm source. Light is picked off at the first beam sampler to stabilise by PDH locking to a cavity.

lock the peak of etalon transmission to one of the cavity longitudinal mode. This dither consists of periodically varying the etalon spacing with a frequency of around 20 kHz. We must be aware of this dither frequency as the phase modulation leads to the creation of sidebands on our light which can interact with the ion causing unexpected errors in gates. We can observe this dither frequency (and harmonics of it) with our ion via composite pulse experiments, however it is currently not expected to be a limiting source of error in any of our desired interactions we study.

As mentioned, the *Solstis* alone can operate with linewidths of $< 50kHz$, however we push this further by referencing the Ti:Saph output with an ulta high finesse cavity by *Stable Laser Systems* and applying a Pound-Drever-Hall (PDH) lock [**<empty citation>**]. A schematic of our 729-nm system is shown in Figure 2.5. PDH locking requires applying two sidebands via an electro-optical modulator (EOM) to the light and directing it onto the stable cavity. The light reflected from the cavity is then directed onto a fast photodetector (*Thorlabs PDA10A2*). The reflection from the cavity consists of the interference between the
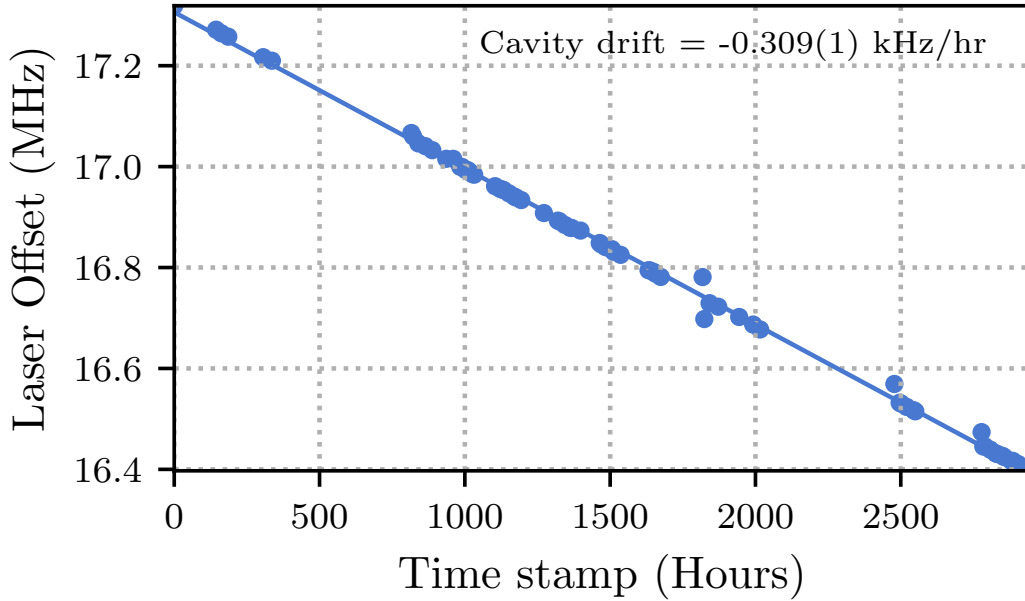
Figure 2.6: Cavity drift over 125 days. Extracted by reference to ion transition.

carrier and the sidebands which have been respectively altered by the cavity transfer function. The photodetector signal is mixed down with the same oscillator signal as provided to the EOM but delayed by some chosen phase, and finally low pass filtered to produce a signal for use as the error signal in the servo loop. This error gives a measure for how far the carrier frequency is from the stable cavity resonant frequency and is used for feedback onto the control AOM situated after the Solstis. The electronics for this control loop are provided also by Stable Laser Systems in the form of their *FPGA Servo* lock box. For an effective PDH lock, we require both short and long term stability of our reference cavity. To ensure the cavity is insensitive to the environment, it is made of an ultra low expansion material. We temperature stabilise the cavity at the zero crossing temperature of 30.6°C, and it is further isolated by being stored in a vacuum system at $< 1e - 7$ mbar. We measure a long term cavity drift of 309(1) Hz/hr over 125 days, seen in figure 2.5. This measurement uses the ion as a frequency reference to probe the cavity frequency and is discussed in section .1.2.

Figure 2.5 displays the other beam paths for our 729-nm system. Some light is

picked off and sent to a wavemeter to continuosly monitor the frequency. However, the majority is coupled to two output fibres for our experiment and another within the group. We transport the 729-nm light from a dedicated laser lab to a room containing the trap apparatus by a 10 m single mode polarization maintaining fibre (*SKXXX*). The fibre is beneficial in cleaning up the mode from the Ti:Saph, however it can introduce phase noise due to mechanical and thermal effects along the 10 m length. To remove this introduced noise we utilise passive stabilisation in the form of thick foam tubing along the fibre length as well as active stabilisation by popular fibre-noise-cancellation technique [**XXX**]. This topic has been discussed extensively in multiple PhD and Masters theses [**XXX**], and so here we only quote the relevant control aspects of our arrangement. We use the *Sinara Stabilizer* [**XXX**] board, a dual channel PID microcontroller, with the *Pounder* [**XXX**] mezzanine board, a dual channel PDH lock generator. The FNC PID software was developed by Ayush Agrawal [**XXX**]. A comparison of spin coherence times is shown in section 3.2.2 with and without fibre noise cancellation enabled.

2.4.2   Single Addressing System

A unique feature of our system is the ability to produce standing wave single ion addressing. The design of this system is shown in figure 2.3. A single ion addressing system must be able to illuminate selected ions in the crystal whilst the others remain unperturbed. The advantage of single addressing, other than ion selectivity, is the increased intensity of light due to the tight waist at the ion location.

Our ions will be separated by a distance $d \approx 5 \ \mu$m. Focussing a collimated 729-nm beam with an objective lens of NA = 0.6 onto the ion provides $\omega_0 = 386$ nm. Abberations present in real optical components will cause the addressed spot to be increasingly non-gaussian and lead to unfavourable cross talk at the neighbouring ions. Therefore care is taken in the optical design.

To produce more than one addressed spot and to steer the spots along the ion

crystal, we use Acousto-Optical-Deflectors[14] (AODs) [12–14]. The beam deflection angle is proportional to the drive frequency supplied to the AOD.

---

[14]ISOMET OAD1343-XY-T70S

3

Experiment Characterisation

Contents

Before we can dive into running novel experiments involving the motion and spin of the atoms, we need to characterise our apparatus. This allows us to both benchmark our system against state of the art results, and to reveal any current limitations of the apparatus which we may need to address.
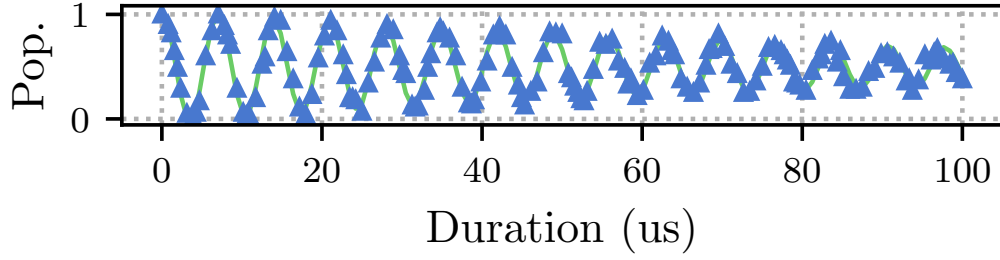
Figure 3.1: Long duration Rabi Flop with fitted decaying flop.

3.1   Quadrupole Transitions

3.2   Spin

3.2.1   Rabi and Ramsey Scans

Here we briefly describe the method in which we extract Rabi frequencies and single qubit gate durations. Long Rabi flop (100 us), fit out carrier frequency of 2*pi*0.0716(1) MHz and Decay rate of 0.0107(7) 1 / us. See long flop. This is 1 mW of power on m1_m3 transition before we changed polarization. Fit with decaying cos function

$$\frac{1 + e^{-\lambda t}\cos(2\Omega t)}{2}, \tag{3.1}$$

3.2.2   Spin Coherence Times

Individual gate fidelities are ultimately limited by loss of coherences of the two qubit states due to either dephasing or by the natural lifetime of the upper level. By our choice of ion and qubit levels, defined between the ground $4S_{1/2}$ state and the metastable $3D_{5/2}$ state, we can expect a lifetime limited coherence time of $\tau = 1.1$ s [**<empty citation>**]. In practise, mainly due to imperfect tracking of laser frequency and magnetic field drifts (as mentioned above), we see coherence times dominated by dephasing. To discern between these two noise sources, we may exploit the fact that we have multiple Zeeman levels within our $3D_{5/2}$ state with varying magnetic field sensitivities. We also have the ability to define our qubit on

the Zeeman split ground state, which decouples dephasing due to the laser from measured coherence times. We perform Ramsey scans with varying mid-sequence delay durations to extract the coherence times, an example of which can be seen in figure **??**. In characterising the spin coherence times, we hope to explore both the efficacy of the magnetic shielding surrounding the ion trap, as well as the stability of the 729 nm laser.

Figure **??** shows how the magnetic shielding effect coherence times of three transitions, XX, YY and ZZ, with magnetic field sensitivities of XX, YY and ZZ respectively. From this we find that without the shielding, we are strongly limited by external magnetic field noise, and with full sheilding we suppress this noise to where we are dominated by laser phase noise. To find the factor by which the magnetic field noise is attenuated, we can compare the coherence times of the laser phase insensitive transition with and without the box. We find an attenuation factor of XX, which is XXconsisitent with the expected attenuation factor of the mu-metal shielding.

With the shiedling in place, we compare the coherence times of the $4S_{1/2}, m_j = -1/2 \leftrightarrow 3D_{5/2}, m_j = -5/2$ with fibre noise cancellation (see section 2.4.1) and without, figure **??**. We find that the coherence time is improved by a factor of XX, with FNC enabled. Our current spin coherence time of XX ms is limited by the laser phase noise, and we expect to be able to push this to [ref R. Oswald] by improving the laser PDH stability. However, for the immediate planned experiments (see section **??**), these improvements will be a low priority due to other likely dominating error sources in the motion of our ions.

3.2.3   State Preparation and Measurement

To utilise two levels of the ion as a qubit, we need to be able to selectively prepare the ion into one of the Zeeman levels of the ground state. As mentioned in section 2.2, we are operating at a low magnetic field of 5 G, leading to a splitting between the Zeeman levels of less than 21 MHz, the natural linewidth of the 397 nm transition.

This means we cannot optically pump using 397 nm frequency selectivity. Further, due to the constraint of beam geometry from the in vacuum optics, we can not use polarisation selectivity of the 397 nm transition. Instead, we use the narrow line width 729 nm laser on resonance with the $4S_{1/2}, m_j = +1/2 \leftrightarrow 3D_{5/2}, m_j = -3/2$ transition, and the 854 nm deshelving laser on resonance, to optically pump into the $m_j = -1/2$ Zeeman level we define as our qubit ground state.

To measure the qubit state of the ion, we apply the 397 nm and 866 nm lasers and count 397 nm photons scattered. From the level diagram shown in figure **??**, we can see that upon turning on the 397 nm laser, if we are in $|0\rangle$, photons will be scattered, and if we are in $|1\rangle$, then no photons will be scattered. To optimise the fidelity of measurement we ensure that the signal is discernible with low error from any background counts on the camera. In general, improving the number of signal counts can be achieved by tuning the 397 nm laser near to the transition resonance, by increasing the readout duration, or by increasing the percentage of scattered photons captured by the imaging system. Practically we desire that the readout step does not heat the motion of the ion and so we red detune the 397 nm laser to a similar setting as for Doppler cooling (see section 3.3.1). The parameters we use for readout are summarised in table **??**, and a typical histogram of readout counts for one and two ions can be seen in figure **??**. We find that the readout fidelity is XXX.

To measure the effect of state preparation and measurement error on longer experimental sequences, we will discuss randomised benchmarking in the following section 3.2.4. Due to the relevance here, we quote the measured state-preparation and measurement error (SPAM) of $\epsilon_{SPAM} = 1.46(6) \times 10^{-3}$.

3.2.4   Randomised Benchmarking

High fidelity unitary operations (gates) are essential for both near intermediate scale quantum computing and for reducing overheads in required physical qubits and
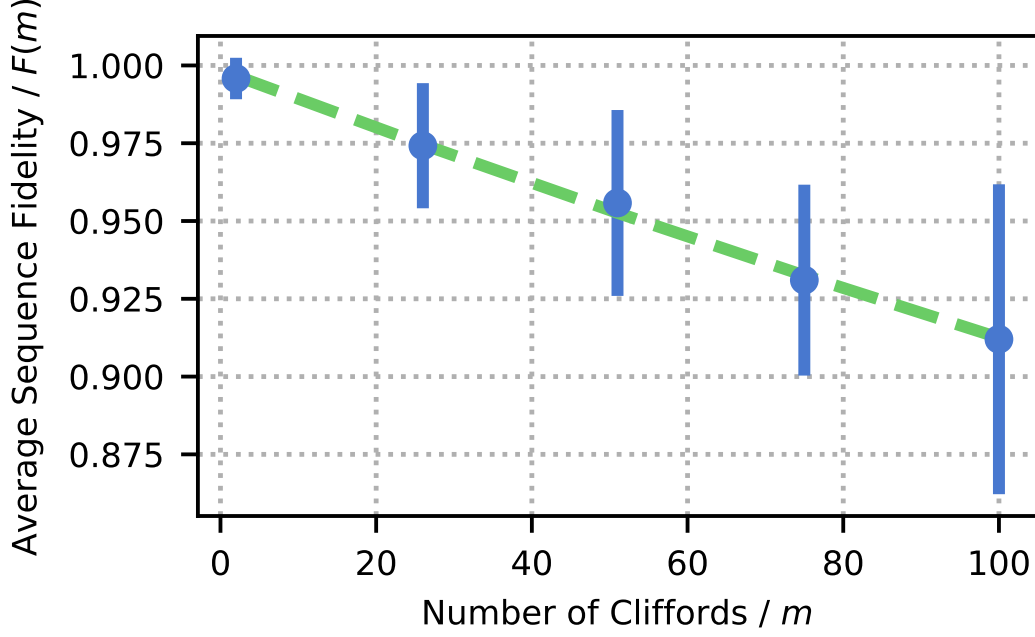
Figure 3.2: RBM fit

operations in fault-tolerant schemes [15]. To evaluate the quality of both our state-prep and single qubit rotations, we employ randomized benchmarking (RBM) [16, 17]. RBM consists of applying random combinations of a pre-chosen discrete set of gates to estimate an average error per gate. We chose the single-qubit Clifford group as our set of gates to evaluate. The single-qubit Clifford group is the set of unitaries which map the Pauli matrices to one another through conjugation. This can be thought of as the complete set of rotations of the Bloch sphere such that all valid combinations of the axis $(x \rightarrow \{\pm x, \ \pm y, \ \pm z\})$, $(y \rightarrow \{\pm x, \ \pm y, \ \pm z\})$, $(z \rightarrow \{\pm x, \ \pm y, \ \pm z\})$ are realized. There are 24 unitaries in this set. We followed the RBM protocol described in the Thesis [18] to evaluate our single-qubit gates. First the qubit is prepared in some known initial state, i.e. prepared in some chosen basis. A gate sequence is then applied which consists of multiple random Clifford gates followed by a final 'inverting' Clifford, where the 'inverting' Clifford is chosen such that the full sequence performs the Identity operation. The state is then measured in the same basis to find any deviations from the Identity being performed due to gate errors. This is repeated with the same preparation and sequence multiple times to calculate the probability

that the Identity was performed - thus giving the sequence fidelity. These steps are repeated for many different random sequences with a range of sequence lengths. The decay model we fit to the fidelity versus number of Clifford gates is given by,

$$F(m) = \frac{1}{2}\left(1 + (1 - 2\epsilon_{SPAM})(1 - 2\epsilon_c)^m\right),\tag{3.2}$$

where $F(m)$ is the fidelity of the sequence of length m, ϵ_{SPAM} is the state-preparation and measurement error, and ϵ_c is the average error per Clifford gate. We use this method to bench mark our qubit transition. The Clifford gates are decomposed into sequences of $\pi/2$ and π pulses about either the $x-$ or $y-$axes. We probe up to $m = 100$ Clifford gates, and fit the decay of the fidelity to the above model. We measure the error per Clifford to be $\epsilon_c = 9.5(3) \times 10^{-4}$, while the SPAM error is $\epsilon_{SPAM} = 1.46(6) \times 10^{-3}$. The decay plot for this RBM sequence can be seen in figure **??**. The error bars are given by the standard deviation of the survival populations. There are on average 3.50 $\pi/2$ pulses per Clifford, with a typical $\pi/2$ duration of 1.3 μs.

3.3 Motion

3.3.1 Cooling

For any interaction involving the motion of the ion, we require both the ability to prepare the motional state with high fidelity, and to subsequently measure this motional state to verify correct preparation. For entangling gates, and the creation of squeezed states which we are considering in this chapter, we assume that we begin in the motional ground state, or in other words, Fock state zero. Our initially trapped ions will be in some high temperature thermal state, (*given by the oven temperature and the PI laser momenta kicks*). We first doppler cool our ions, and then subsequently sideband cool them. We give a brief description of these two cooling processes here.

Doppler Cooling

Doppler cooling exploits the fact that incident light onto a moving ion will appear frequency shifted in the rest frame of the ion. For Doppler cooling of ^{40}Ca$^+$, we apply both the 397 nm and 866 nm lasers. We initially red detune the 397 nm laser by around 100 MHz. This results in the preferential absorption of a quanta of 397 nm light by ions with a velocity vector antiparallel photon k-vector. After this absorption, the ion will be in the excited $4P_{3/2}$ state and spontaneously decay to either the $4S_{1/2}$, or the $3D_{3/2}$ emitting a photon of either 397 nm or of 866 nm respectively into a random direction. These two decay paths have a branching ratio of XX. As we desire many photon kicks to cool our ions, we repump the electron out of this metastable $3D_{3/2}$ level by applying an on resonant 866 nm beam. The absorption and sequential emission of this 397 nm photon will lead to a net reduction in the motional energy of the ion if the photon is emitted at a higher energy than when absorbed. The equilibrium temperature is given by the condition where the doppler cooling rate is equal to photon recoil heating of the ion. Assuming a Lorentzian absorption profile, the minimum temperature is given by,

$$T_{Doppler} \approx \frac{\hbar\gamma}{2k_B}, \tag{3.3}$$

where $\hbar$ is the reduced Planck constant, γ is the natural linewidth of the transition, and k_B is Boltzmann's constant.

For ^{40}Ca$^+$, the natural linewidth of the 397 nm transition is $\frac{\gamma}{2\pi} = 21$ MHz, leading to a Doppler temperature of approximately 0.5 mK. Given a radial mode frequency of $\frac{\omega}{2\pi} = 4$ MHz, and the mean occupation number of the oscillator being given by,

$$\bar{n} = \frac{1}{e^{\hbar\omega/k_B T} - 1}, \tag{3.4}$$

we find the final thermal distribution to have an expected Fock state of $\bar{n} = 2.3$. Using parameters summarised in table **??**, we find practically the final temperature after Doppler cooling to be around XXX mK.
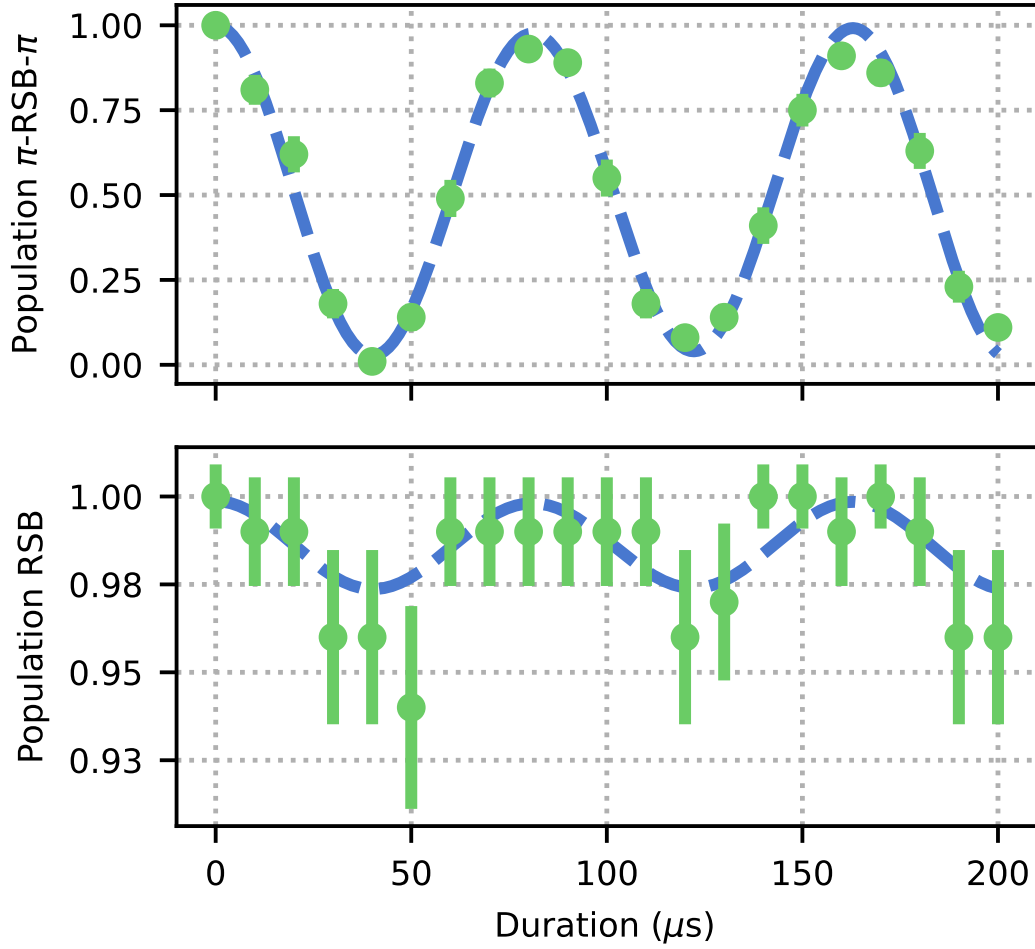
Figure 3.3: Thermometry after sideband cooling.

Sideband Cooling

To further cool the ions toward their motional ground state, we use resolved sideband cooling. The motion of the ion, described by a harmonic oscillator, modulates the transition frequencies of the ion, leading to sidebands at multiples of the motional frequency. For the $4S_{1/2} \leftrightarrow 3D_{5/2}$ transition, at appropriate laser intensity and motional mode frequencies, these sidebands can be resolved spectroscopically. The pulsed sideband technique we employ consists of red sideband pulses, followed by deshelving, and repumping pulses on the 854 nm and 866 nm transitions respectively. An example pulse sequence can be seen in figure **??**, and experimental parameters
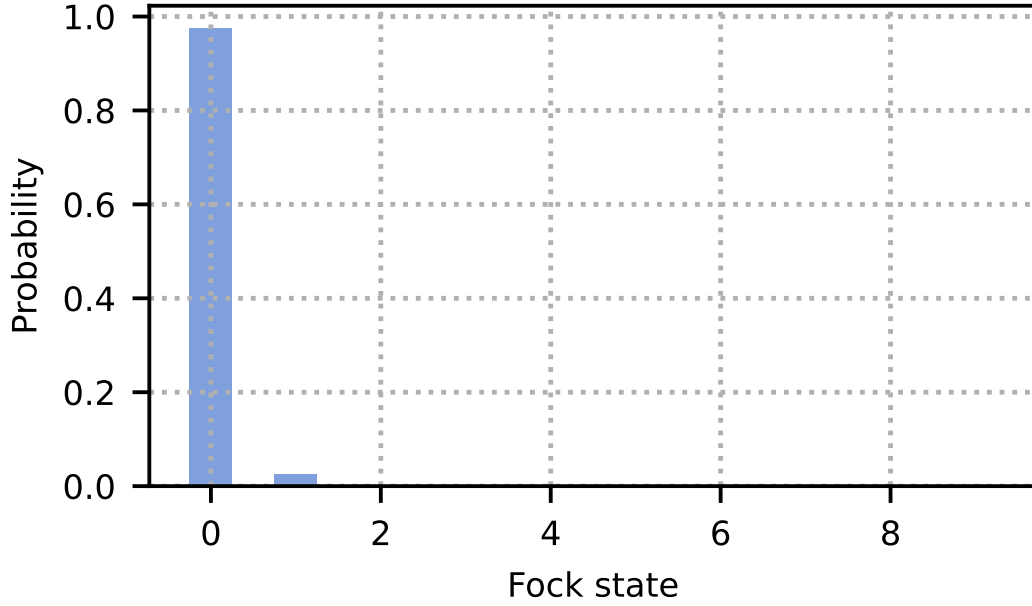
Figure 3.4: Fock state distribution

we use are summarised in table **??**.

To verify the efficacy of our sideband cooling, we perform thermometry experiments by driving on resonance red sideband (RSB) and pi-RSB-pi pulse sequences. We record the time dynamics of population flopping as we vary RSB pulse length. In the case of Fock state zero, we expect to see a strong signal on the RSB, and no signal on the pi-RSB-pi pulses. We fit a thermal Fock state distribution (with truncation at Fock state = 100) to these signals to extract the mean occupation number, and $\eta\Omega$, the carrier Rabi frequency multiplied by the Lamb-Dicke parameter. A typical thermometry scan after Doppler and sideband cooling can be seen in figure **??**. We find that the mean occupation number after sideband cooling is $\bar{n} = 0.03()$, and $\eta\Omega = XX$ MHz.

Optimisation of the cooling parameters can be roughly performed by fitting temperature while scanning RSB pi-pulse durations, total number of pulses, repumping and deshelving times. One can optimise for minimum temperature, however it is also important to optimise for total cooling duration. For single ion, single mode experiments, this duration is often a non-issue, however for multi-ion crystals, any
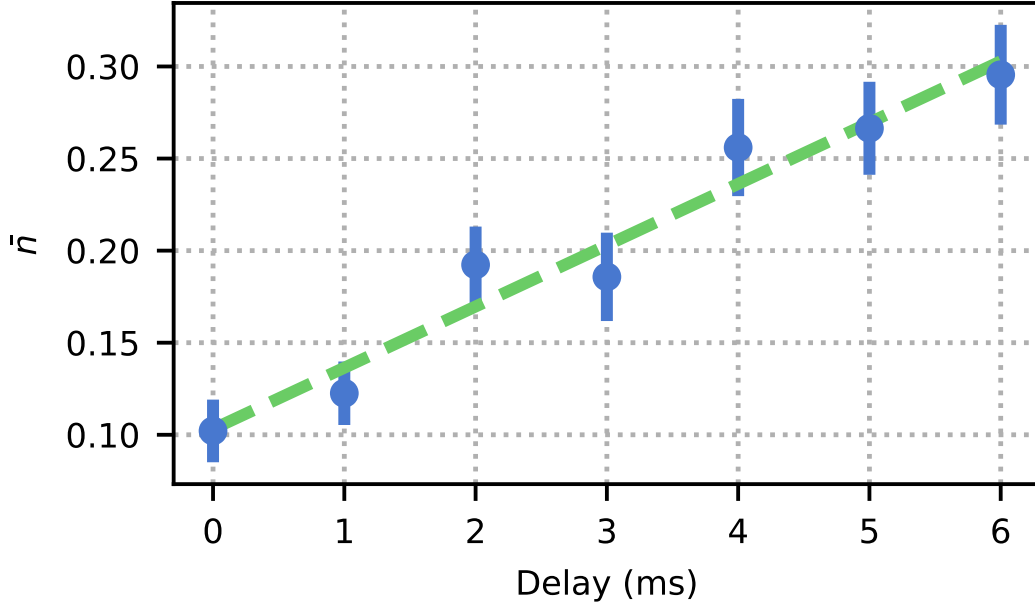
Figure 3.5: Heating rates of upper radial mode.

interaction involving the motion, may require the sequential sideband cooling of multiple motional modes. This can not be easily parallalised due to the requirement that the RSB pi-pulse is performed near resonance to one of the motional sidebands. This sequential cooling strategy can be either limiting when heating and cooling rates are comparable, or in the best case, painful due to long data collection times. To mitigate this issue, other sub-Doppler cooling techniques with larger accepted frequency bandwidths may be employed. Examples are dark-resonance cooling[], and electromagnetically induced transparency (EIT) cooling[], and Sisyphus cooling[]. These techniques are not yet implemented in our system, but will be likely additions once we move to larger ion crystals.

3.3.2 Heating Rates

As mentioned, the cooling of our ions is only relevant if we have acceptable heating rates. Heating of the motion is predominantly caused by the ion trap itself. This can be due to imperfections in the surface of exposed dielectric and metals causing

stray fields, or can be due to noise on the DC and RF drive voltages[]. Noise due to the surface of the trap can be mitigated by increasing ion-electrode distances, or by using traps with smaller surface area direclty exposed to the ion. In our case, as mentioned in sections 2.1, the NPL trap has an electrode ion distance somewhat larger than most surface traps, but less than that of a macroscope blade or rod style trap. To verify the heating rate of our system, we performed a series of thermometry scans whilst varying some delay time between cooling and thermometry pulses. A typical plot can be seen in figure **??**. We find that the heating rate of our system is approximately 33(3) quanta per second on the upper radial 4 MHz mode on one ion.

It is expected that the heating rate will be larger for lower frequency motional modes if we assume uniform electric field noise. We also verify this by looking at heating rate on the radial mode while varying the axial mode frequency. This is a useful diagnostic to check for unexpected heating at certain frequencies, perhaps due to RF noise in the lab. We find....

3.3.3   Motional Mode Stability

3.3.4   Motional Coherence Times

We will utilise the motional modes of the ion to store quantum information. As with the section on spin coherence times 3.2.2, the fidelity of operations, and success probability of algorithms will be limited by the coherence time of the motional state. To measure motional coherence, we perform a Ramsey sequence between states $|\downarrow, 0\rangle$ and $|\downarrow, 1\rangle$, where the first element is the qubit state, and the second element is the motional Fock state. To prepare these states we apply the following pulse sequence:

- State prep system to $|\downarrow, 0\rangle$ via optical pumping and SBC.

- Apply $\pi/2|_y$-pulse on carrier transition to prepare the qubit in $|+, 0\rangle$.

- Apply π-pulse on the RSB to prepare the motional state in $|\downarrow, 0\rangle + |\downarrow, 1\rangle$.
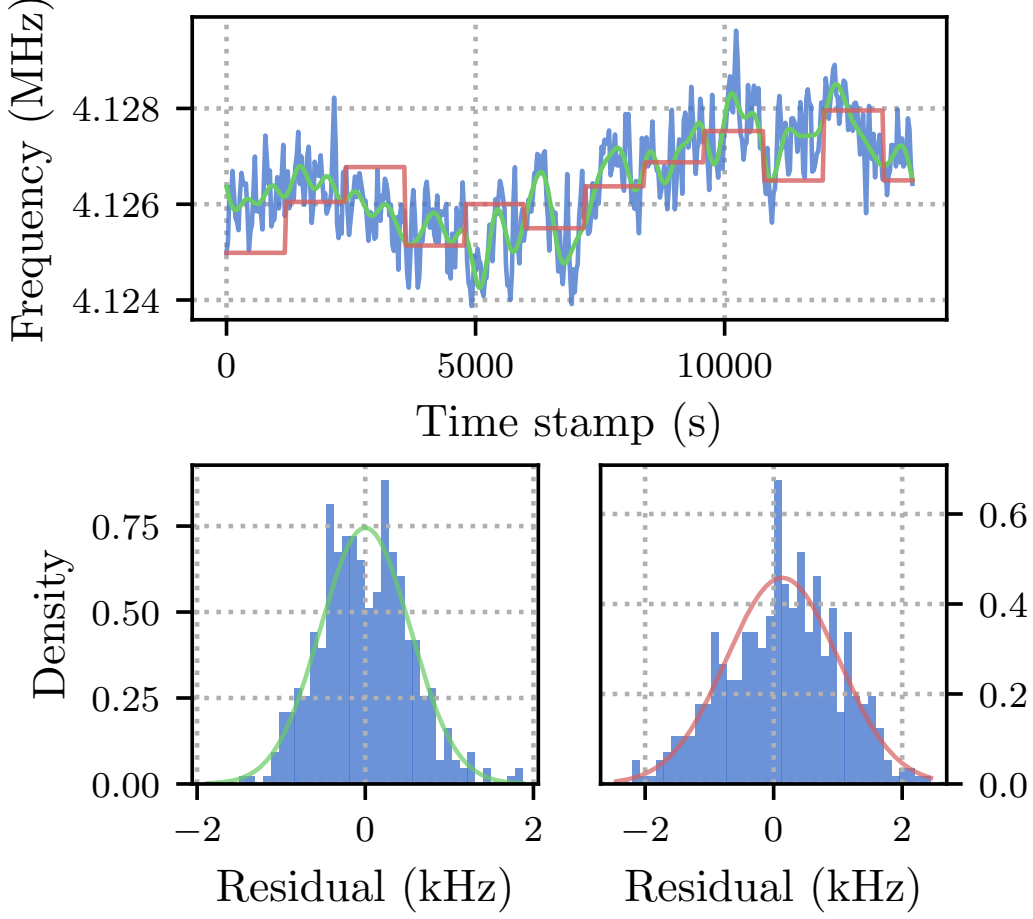
Figure 3.6: Motional mode frequency drift.

The full Ramsey sequence is then completed by delaying for some time t, and then reversing the above state prep and measuring spin population in $|\downarrow\rangle$.

There are two main mechanisms for motional decoherence: motional heating, as characterised in section 3.3.2, and motional dephasing due to mode frequency instability, as discussed above.

A heating rate dominated coherence time is given by, $\tau_{\text{HEAT}} = (\sqrt{e} - 1)/\dot{\bar{n}}$ [**XXX**], where $\dot{\bar{n}}$ is the heating rate. A dephasing dominated coherence time, consisting of the motional mode frequency drifting shot-to-shot with a standard deviation σ, is characterised by a Gaussian decay profile with a coherence time of $\tau_{DEPH} = \sqrt{2}/\sigma$.

Evaluating both of these models with $\dot{\bar{n}} = 33(3)$ q/s, and $\sigma/(2\pi) = 750$ Hz, we find expected motional coherence times of $\tau_{\text{HEAT}} \approx 20$ ms and $\tau_{\text{DEPH}} \approx 0.3$ ms respectively. From these auxiliary characterisations of the motional modes, we then expect to be in the dephasing dominated regime. However, as can be seen in figure **??**, we experimentally find a motional coherence time of XX(X) ms by fitting a Gaussian decay.

Assuming this was dominated by motional mode drifts between shots, we can estimate the motional mode drift standard deviation, $\sigma/(2\pi) = 225$ Hz. Comparing this to the previously measured long-term motional mode stability, we see a discrepancy. This is likely due to the issue of time scales. The motional mode stability in the described Ramsey experiment is only relevant over the time it takes to collect enough statistics for one fringe scan, around 1 second. However, the above motional mode stability is probed only every 20 seconds and so may overestimate the instability over shorter time scales.

Work must be done to estimate the fast motional noise, however, first there may be simple improvements that can be made to the RF chain to improve both short and long term motional mode stability. These improvements are described in section 2.1.1.

3.4   Spin-Dependent Forces

For full control of the spin-motion hybrid system, we require interactions that couple the two. Perhaps the simplest of this class of interactions are the red- and blue-sidebands (RSB and BSB respectively). The RSB interaction was used previously in the thermometry and sideband cooling sections 3.3.1. The RSB (BSB) consists of a single frequency laser tuned at the carrier frequency minus (plus) the motional mode frequency, ω_m. The interaction is well described by the (Anti-) Jaynes-Cummings Hamiltonian, and effectively couples spin flips with the addition or subtraction of a motional quanta depending on the initial spin state. Here we introduce another such interaction coupling spin and motion, known as the spin-dependent force. If

the RSB and BSB interactions couple spin-motion in the motional Fock basis, then the SDF couples the two in a motional coherent basis. The SDF displaces the motional state in phase space, with a direction dependent on the spin state and an effective detuning parameter.

We use the optical Mølmer-Sørensen (MS) scheme [**<empty citation>**], to generate the SDF via a bichromatic laser field. Bichromatic refers to the simultaneous application of two tones symmetrically detuned around the qubit carrier frequency, with absolute detuning approximately equal to the motional mode frequency, $\delta \approx \omega_m$. The resulting interaction, when ignoring off resonant and higher order couplings, is given by,

$$\hat{H}_{MS} = \hbar\eta\Omega \ \hat{\sigma}_\phi \cos(\delta t) \left(a e^{-i\omega_m t} + a^\dagger e^{i\omega_m t} \right), \tag{3.5}$$

where η is the Lamb-Dicke parameter, Ω is the carrier Rabi frequency, $a(a^\dagger)$ is the lowering (raising) operator, and σ_ϕ is the Pauli operator with ϕ being in the x, y -plane. Applying the rotating wave approximation, and defining $\delta_g = \delta - \omega_m$, we find that the interaction Hamiltonian can be approximated to,

$$\hat{H}_{MS} = \frac{\hbar\eta\Omega}{2} \ \hat{\sigma}_\phi \left(a e^{-i\delta_g t} + a^\dagger e^{i\delta_g t} \right). \tag{3.6}$$

We may control the trajectory of this displacement by varying δ_g: on resonance, $\delta_g = 0$, we see linear trajectories, whilst off resonance, $\delta_g \neq 0$, we see cyclic trajectories where after some time $t = 2\pi/\delta_g$, the motion returns to the initial state (with perhaps some phase shift). We shall exploit this control in both the two-qubit entangling gate experiments, as well as in the creation of squeezed states.

3.4.1 Calibrating the SDF

The MS interaction is widely used in ion trap experiments due to it being robust against varying intial motional states, and to the effects of heating during the pulse sequence. However, in our use case, the SDF is sensitive to various frequency and power miscalibrations and drifts of these between calibrations. Here we describe
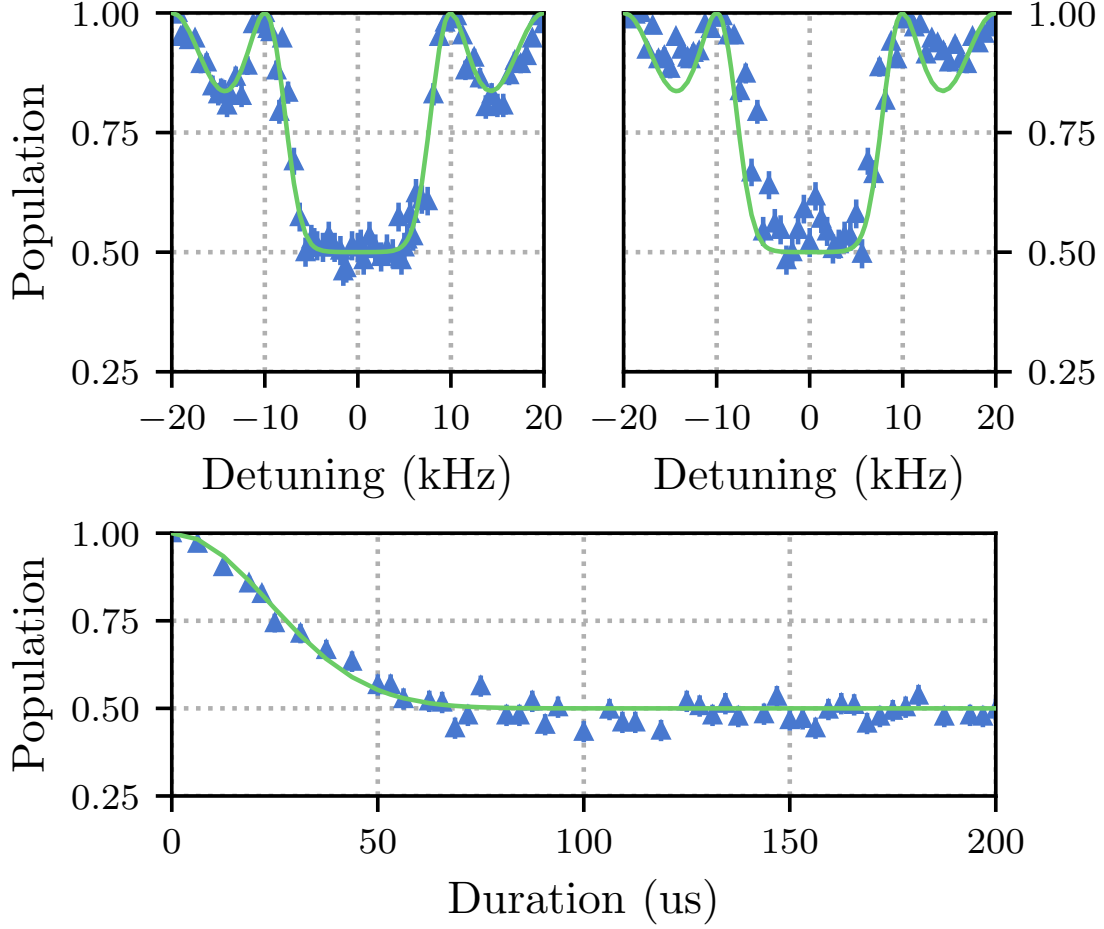
Figure 3.7: SDF traces.

briefly the work flow for calibrating and optimising the SDF behaviour.

In honesty, there are not many moving parts in the SDF interaction, we must know the central qubit frequency, the motional mode frequency, the power in each tone, and the durations of the pulses. Complications come from the reality that we have a multi-level system, multiple motional modes, and that experimentally each parameter can only be controlled to a certain precision.

We negate the effect of nearby motional modes by either selecting our interaction mode to be well seperated from the others either in frequency or geometrically, by operating the SDF near to resonance of the desired mode, or by using pulse shaping to ramp the power of the SDF and suppress the off-resonant excitation of these

other modes. There are many tricks to either mitigate or exploit the effects of these other modes, and we will not go into detail here.

The power balance of the SDF tones is complicated due to our use of AOMs. AOMs generate frequency shifts in the laser beam at the expense of small frequency-dependent angular shifts. We couple the beam after the AOM into a single mode fibre (see figure 2.5), and so the AOMs effectively introduce a frequency-dependent loss. To calibrate the power balance we look at a pick off of the bichromatic beam before the ion on a high bandwidth photodiode. We measure the beatnote contrast of the two tones and optimise the power balance to maximise this contrast.

The far off-resonant levels of our ion lead to light-shifts of our qubit frequency. Practically to account for the light-shift we must calibrate this central frequency at the optical power we use in the interaction. We do this with the SDF interaction itself. When the qubit frequency is set incorrectly, the two tones will no longer have the same absolute detuning from their respective RSB or BSB. This manifests as a "skewness" of the SDF detuning trace, an example of such can be seen in figure 3.7. By varying the qubit frequency and inspecting these detuning scans, the desired SDF behaviour can be found.

To verify the behaviour of our calibrated SDF with theory, we use both "detuning" and "duration" scans. The "detuning" scan is performed by varying the detuning, δ_g, of the interaction, whilst the keeping the SDF duration, t, constant, and vice-versa for the "duration" scan.

Figure 3.7 shows the measured duration scan with a fit given by,

$$P_{\downarrow,\text{th}} = \frac{1}{2}\left[1 + e^{-4\left(\bar{n}+\frac{1}{2}\right)|\alpha(t)|^2}\right], \tag{3.7}$$

where we assume we begin in a thermal state with average Fock state $\bar{n} = 0.03$ which we found previously from thermometry measurements. Here the displacement, $|\alpha(t)| = \Omega_{\text{SDF}}t/2$, where Ω_{SDF} is the SDF amplitude. These measurements were performed with a duration of XX ms, total power of xx mW, $\delta_{\text{LS}} = 2\pi \times XX$ kHz. We find $\Omega_{\text{SDF}} = 2\pi \times 6.6(2)$ kHz, from the measured fit, which is in good agreement with the expected value of $\Omega_{\text{SDF}} = \eta\Omega_{\text{CAR}}$, where Lamb-Dicke parameter $\eta = 0.05XXX$

and $\Omega_{\text{CAR}} = 2\pi \times 132$ kHz XXX measured from Rabi flopping at 15XXX mW. The detuning scan, shown in figure 3.7, is fitted by taking the displacement to be $|\alpha(t)| = \Omega_{\text{SDF}} \sin(\delta t/2)/\delta$. Here we qualitatively see a good agreement between the measured data and the expected behaviour, with the main important features being the "closure" at $\delta = 2\pi/t$ where the motional state returns to the initial state, and the central flat region around $P_{\downarrow,\text{th}} = 0.5$ where the two motional wave packets are non-overlapping.

3.5 Two-Qubit Entangling Gates

We perform two-qubit entangling gates using the Mølmer-Sørensen (MS) interaction [**<empty citation>**]. This interaction is the same described SDF from the previous section, but applied globally to two ions. The MS interaction relies on the spin dependent geometric phase accumulated during the motional displacement. To create a two-qubit entangled state, a differential geometric phase of $\pi/2$ must be accumulated between the two-qubit basis states. To ensure there is no residual motional entanglement, the final motional state must return to the initial state. In practise, using an SDF detuned by δ_g, this is achieved by applying the MS interaction for a time $t = 2\pi/\delta_g$. The MS gate is a universal two-qubit gate, and along with only single qubit gates, constitutes a universal gate set for discrete quantum algorithms.

Here we quote the fidelity of experimentally demonstrated two-qubit gates on our system. The fidelity serves to quantify the "closeness" or similarity of two density matrices. For the use case of quantum information processing, what we care about is that the experimental unitary applied in the gate sequence closely resembles the unitary we desire theoretically. In general this means that we should measure the fidelity of the applied unitary in an input state agnostic way. Unfortunately this is often not practical as the input state space can be unwieldly, and the act of preparing the input state can also be error prone. As a compromise we can apply
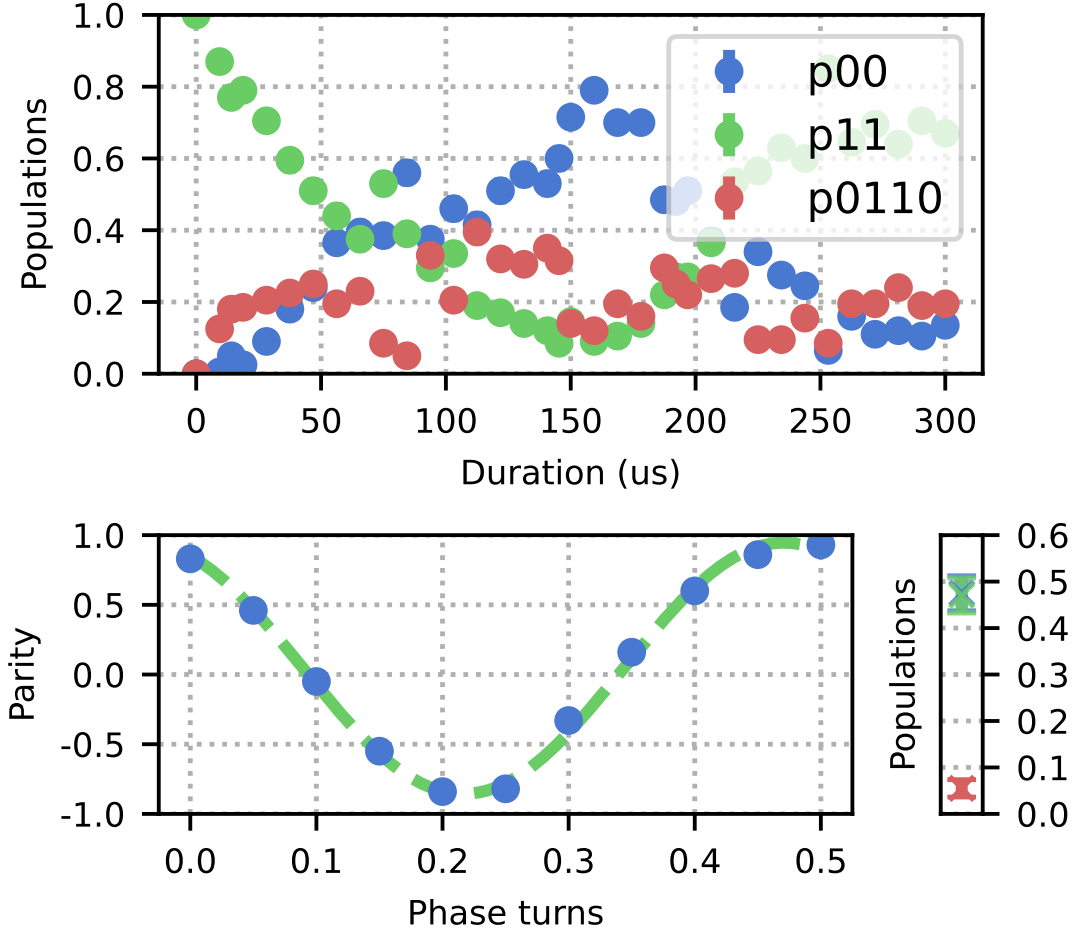
Figure 3.8: MS Gate.

the test unitary to either one, or to a set of input states, and measure the fidelity of the output state with respect to the known target state. If the error mechansims of the test unitary are well understood, arguments can be made that this measured fidelity for a set of input state is representative (or not representative) of the average fidelity over the input state space.

Here for a two-qubit entangling gate, we target the creation of the Bell state $|\Phi^+\rangle = 1/\sqrt{2}\left(|00\rangle + e^{i\phi_0}|11\rangle\right)$, from an initial state of $|11\rangle$. The fidelity between our mixed state ρ, and the pure Bell state may be given by,

$$\mathcal{F} = \langle\Phi^+|\rho|\Phi^+\rangle = \frac{1}{2}\left(\rho_{00,00} + \rho_{11,11}\right) + \frac{1}{2}\left(e^{i\phi_0}\rho_{11,00} + e^{-i\phi_0}\rho_{00,11}\right), \quad (3.8)$$

To extract the fidelity experimentally we follow the popular protocol [**XXX**], where the first bracketted term of equation 3.8 is measured by performing projective measurements of the two ions after the gate sequence to extract populations, and the second bracketted term, known as the coherence terms, are measured by applying a global analysis $\pi/2|_\phi$ pulse to the two ions and applying parity measurements. The contrast of the parity oscillations when varying the phase ϕ of the $\pi/2$ pulse yields the desired coherence term magnitude and phase. We require the creation of a Bell state for two qubit entangling, however do not care what basis this state is in, and so float the target Bell state phase and take only the magnitude of the fitted parity oscillations for calculating the final fidelity.

The best two-qubit entangling gate fidelity currently achieved on our system is $\mathcal{F} = 92(2)\%$. As shown in figure 3.8, the magnitude of the parity scan was measured to be $0.90(2)$, while the populations $(\rho_{00,00} + \rho_{11,11}) = 0.95(2)$. Each population point in these figures are found by taking the average of 200 shots of the gate sequence.

These results serve as both a proof of principle for full spin control on our system, but also as a benchmark to which we can compare future system improvements. For future work, we will require the use of this entangling gate either as Bell state preparation for input to analogue simulation experiments [**<empty citation>**], or as a primitive gate for the spin component of hybrid algorithms [**<empty citation>**]. In both these cases, especially any use that requires multiple concatenated entangling gates, we will likely require improved gate fidelities. It is suspected that we are currenlty limited by nearby hot motional modes, and the lack of pulse ramping in our gate sequence. We expect that with the addition of pulse shaping we will be able to suppress the effect of nearby off-resonant transitions, and by sideband cooling of nearby motional modes we will futher suppress contributions from unwanted spin-motion couplings.

4
Outlook

Appendices

.1 Appendix

.1.1 Generating Ions

.1.2 Extracting Laser Offset and Magnetic Field

.2 Experimental Control

.3 Creating Squeezed States

References

[1] Kaushal Choonee, Guido Wilpers, and Alastair G. Sinclair. "Silicon microfabricated linear segmented ion traps for quantum technologies". In: *19th Int. Confrence on Solid-State Sensors* (June 2017), pp. 615–618.

[2] D. Allcock. "Surface-electrode ion traps for scalable quantum computing". In: *Ph.D. thesis, University of Oxford* (2011). URL: `https://ora.ox.ac.uk/objects/uuid:bfe6d0db-092f-4661-a5c8-da3ed7ff59ff` (visited on 08/25/2023).

[3] D. Kielpinski, C. Monroe, and D. J. Wineland. "Architecture for a large-scale ion-trap quantum computer". In: *Nature* 417.6890 (June 2002), pp. 709–711. URL: `https://www.nature.com/articles/nature00784` (visited on 08/25/2023).

[4] Q. A. Turchette et al. "Heating of trapped ions from the quantum ground state". In: *Physical Review A* 61.6 (May 2000), p. 063418. URL: `https://link.aps.org/doi/10.1103/PhysRevA.61.063418` (visited on 08/25/2023).

[5] Patrick See et al. "Fabrication of a Monolithic Array of Three Dimensional Si-based Ion Traps". In: *Journal of Microelectromechanical Systems* 22.5 (Oct. 2013), pp. 1180–1189.

[6] Guido Wilpers et al. "A monolithic array of three-dimensional ion traps fabricated with conventional semiconductor technology". In: *Nature Nanotechnology* 7.9 (Sept. 2012), pp. 572–576. URL: `https://www.nature.com/articles/nnano.2012.126` (visited on 08/14/2023).

[7] M.J. Madsen et al. "Planar ion trap geometry for microfabrication". In: *Applied Physics B* 78.5 (Mar. 2004), pp. 639–651. URL: `https://doi.org/10.1007/s00340-004-1414-9` (visited on 08/14/2023).

[8] D. J. Berkeland et al. "Minimization of ion micromotion in a Paul trap". In: *Journal of Applied Physics* 83.10 (May 1998), pp. 5025–5033. URL: `https://doi.org/10.1063/1.367318` (visited on 08/25/2023).

[9] K M Birnbaum. "Ultra-High Vacuum Chambers". In: *Useful Notes* (2005).

[10] J. Wolf. "Cryogenic, near-field quantum logic chips with passive field nulling on 43Ca+". In: *Ph.D. thesis, University of Oxford* (2019). URL: `https://ora.ox.ac.uk/objects/uuid:df535734-dc43-487a-93de-b8789929104b` (visited on 08/25/2023).

[11] S. Saner et al. "Breaking the entangling gate speed limit for trapped-ion qubits using a phase-stable standing wave". In: *arXiv* (May 2023), p. 2305.03450. URL: `http://arxiv.org/abs/2305.03450` (visited on 06/26/2023).

[12] W. Nagourney. "Quantum Electronics for Atomic Physics and Telecommunication". In: *Oxford University Press* (May 2014). URL: https://doi.org/10.1093/acprof:oso/9780199665488.002.0003 (visited on 08/25/2023).

[13] Rui-Rui Li et al. "A low-crosstalk double-side addressing system using acousto-optic deflectors for atomic ion qubits". In: *arXiv* (June 2023), p. 2306.01307. URL: http://arxiv.org/abs/2306.01307 (visited on 07/03/2023).

[14] I. Pogorelov et al. "Compact Ion-Trap Quantum Computing Demonstrator". In: *Physical Review X Quantum* 2.2 (June 2021), p. 020343. URL: https://link.aps.org/doi/10.1103/PRXQuantum.2.020343 (visited on 04/28/2023).

[15] A. M. Steane. "Overhead and noise threshold of fault-tolerant quantum error correction". In: *Physical Review A* 68.4 (Oct. 2003), p. 042322. URL: https://journals.aps.org/pra/abstract/10.1103/PhysRevA.68.042322 (visited on 12/20/2022).

[16] E. Knill et al. "Randomized benchmarking of quantum gates". In: *Physical Review A* 77.1 (Jan. 2008), p. 012307. URL: https://link.aps.org/doi/10.1103/PhysRevA.77.012307 (visited on 08/25/2023).

[17] Easwar Magesan, J. M. Gambetta, and Joseph Emerson. "Scalable and Robust Randomized Benchmarking of Quantum Processes". In: *Physical Review Letters* 106.18 (May 2011), p. 180504. URL: https://link.aps.org/doi/10.1103/PhysRevLett.106.180504 (visited on 08/25/2023).

[18] A. C. Hughes. "Benchmarking memory and logic gates for trapped-ion quantum computing". In: *Ph.D. thesis, University of Oxford* (2021). URL: https://ora.ox.ac.uk/objects/uuid:3fdb0b98-3c50-483c-b66e-132495ce71af (visited on 08/19/2023).